Precision scans of the Pixel cell response of double sided 3D Pixel detectors to pion and X-ray beams

2011 JINST 6 P05002

(http://iopscience.iop.org/1748-0221/6/05/P05002)

PUBLISHED BY IOP PUBLISHING FOR SISSA

RECEIVED: *March 14, 2011*
ACCEPTED: *April 21, 2011*
PUBLISHED: *May 5, 2011*

Precision scans of the Pixel cell response of double sided 3D Pixel detectors to pion and X-ray beams

A. Mac Raighne,[a,1] **K. Akiba,**[g] **L. Alianelli,**[b] **R. Bates,**[a] **M. van Beuzekom,**[g] **J. Buytaert,**[d] **M. Campbell,**[d] **P. Collins,**[d] **M. Crossley,**[d] **R. Dumps,**[d] **L. Eklund,**[a] **C. Fleta,**[c] **A. Gallas,**[e] **M. Gersabeck,**[a] **E.N. Gimenez,**[b] **V.V. Gligorov,**[a] **M. John,**[f] **X. Llopart,**[d] **M. Lozano,**[c] **D. Maneuski,**[a] **J. Marchal,**[b] **M. Nicol,**[d] **R. Plackett,**[d] **C. Parkes,**[a] **G. Pellegrini,**[c] **D. Pennicard,**[a] **E. Rodrigues,**[a] **G. Stewart,**[a] **K.J.S. Sawhney,**[b] **N. Tartoni**[b] **and L. Tlustos**[d]

[a] *School of Physics and Astronomy, University of Glasgow, Scotland, U.K.*
[b] *Diamond Light Source Ltd, Oxfordshire, U.K.*
[c] *Instituto de Microelectrónica de Barcelona, IMB-CNM-CSIC, Barcelona, Spain*
[d] *CERN CH-1211, Genève 23, Switzerland*
[e] *Facultad de Fisica, University of Santiago de Compostela, Santiago de Compostela, Spain*
[f] *Dept. of Physics, University of Oxford, Oxford, U.K.*
[g] *Nationaal Instituut Voor Subatomaire Fysica, Amsterdam, Netherlands*

E-mail: a.macraighne@physics.gla.ac.uk

ABSTRACT: Three-dimensional (3D) silicon sensors offer potential advantages over standard planar sensors for radiation hardness in future high energy physics experiments and reduced charge-sharing for X-ray applications, but may introduce inefficiencies due to the columnar electrodes. These inefficiencies are probed by studying variations in response across a unit pixel cell in a 55μm pitch double-sided 3D pixel sensor bump bonded to TimePix and Medipix2 readout ASICs. Two complementary characterisation techniques are discussed: the first uses a custom built telescope and a 120GeV pion beam from the Super Proton Synchrotron (SPS) at CERN; the second employs a novel technique to illuminate the sensor with a micro-focused synchrotron X-ray beam at the Diamond Light Source, UK. For a pion beam incident perpendicular to the sensor plane an

[1] Corresponding author.

doi:10.1088/1748-0221/6/05/P05002

2011 JINST 6 P05002

overall pixel efficiency of 93.0±0.5% is measured. After a 10^o rotation of the device the effect of the columnar region becomes negligible and the overall efficiency rises to 99.8±0.5%. The double-sided 3D sensor shows significantly reduced charge sharing to neighbouring pixels compared to the planar device. The charge sharing results obtained from the X-ray beam study of the 3D sensor are shown to agree with a simple simulation in which charge diffusion is neglected. The devices tested are found to be compatible with having a region in which no charge is collected centred on the electrode columns and of radius 7.6±0.6μm. Charge collection above and below the columnar electrodes in the double-sided 3D sensor is observed.

KEYWORDS: X-ray detectors; Particle tracking detectors (Solid-state detectors); Large detector systems for particle and astroparticle physics

2011 JINST 6 P05002

Contents

1 Introduction **1**
- 1.1 3D double sided sensors 3
- 1.2 Planar sensors 4
- 1.3 Medipix2 and TimePix ASICs 4

2 Pion beam **5**
- 2.1 Experimental set-up 5
- 2.2 Analysis and track reconstruction 6
- 2.3 Landau distributions 7
- 2.4 Efficiency distributions at normal incidence 8
- 2.5 Efficiency distributions at angles 11
- 2.6 Single pixel efficiency versus threshold 11
- 2.7 Charge sharing 12
- 2.8 Conclusions 13

3 X-ray synchrotron radiation **14**
- 3.1 Experimental set-up 14
- 3.2 Alignment procedure 15
- 3.3 Background analysis 16
- 3.4 Efficiency maps 16
- 3.5 Charge sharing 18
- 3.6 Conclusions 20

4 Discussion **21**

2011 JINST 6 P05002

1 Introduction

Future High Energy Physics (HEP) and synchrotron X-ray experiments require a new generation of detectors capable of high-speed readout, operation under extreme radiation fluences, and that cover large areas with minimal dead space. The 3D sensor design offers several advantages over the planar silicon sensor design and is a strong contender for such future detection systems.

The 3D sensor architecture [1] differs from a standard planar sensor design by having columnar electrode structures created in the sensor substrate rather than on the device surfaces, as illustrated in figure 1. The distance between electrodes in the planar device is defined by the sensor thickness. This is no longer the case in the 3D design where the electrodes can be brought closer together significantly reducing the charge collection time of the device, and reducing the required bias voltage. A faster collection time reduces the trapping effect of radiation induced defects and

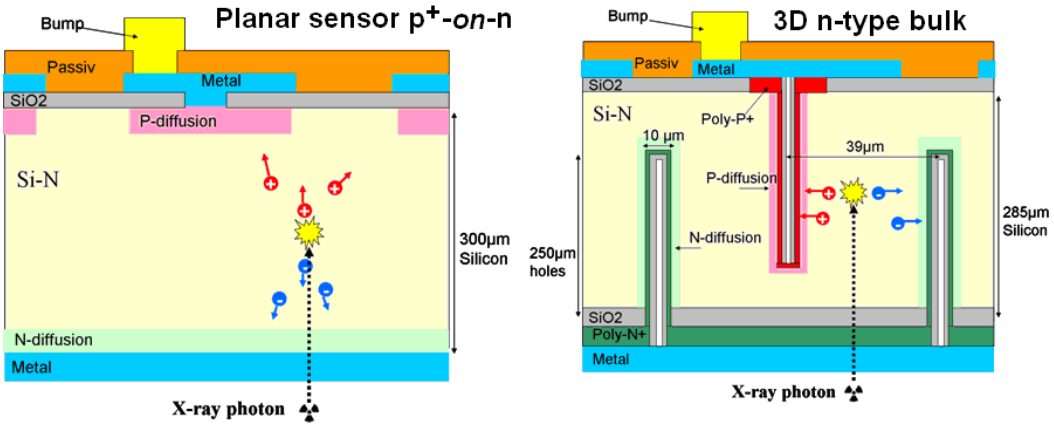

Figure 1. Schematics of the (a) planar and (b) 3D double-sided sensors.

therefore increases the detector's charge collection performance after heavy irradiations [2] making the detector design attractive for applications in future high energy particle tracking experiments.

The electrode structure of the 3D design defines an electric field within the substrate that differs from that of the planar sensor. In the planar design charge created in the substrate drifts through the substrate thickness towards the collecting electrodes on the surface of the device. This allows time for the charge cloud to spread laterally by diffusion, leading to a greater probability that the charge will be collected across multiple pixels. The electric field in the 3D design drifts charge parallel to the substrate surface, towards the collecting electrode in each pixel cell. This reduces the charge sharing in the detector which is advantageous to X-ray imaging applications. In imaging applications, where photon counting is used, charge sharing can lead to multiple counts or no counts for a single photon depending on the threshold thus reducing the image quality. The 3D electrode structure has a self-shielding geometry which reduces the required guard ring area and can also allow for active edge technology [3] to be applied. Consequently, the size of the insensitive region around the sensor can be reduced to a few microns. This is important in large area detectors where multiple sensor substrates are tiled together. The possibility to cover large detection areas with minimal dead area, the fast collection times and the reduction in charge sharing makes 3D detector designs attractive for application in synchrotron X-ray experiments as well as high energy physics.

However, 3D sensors are more complex to manufacture than planar sensors. They have a higher capacitance per pixel [4] and, as discussed in this paper, they may suffer from inefficiencies due to the electrode columns.

We report in this paper the response of 3D double-sided pixel sensors [4], figure 1(b), and traditional planar pixel devices, figure 1(a), to both X-rays and high energy pions. Both devices are bump bonded to TimePix and Medipix2 pixel readout ASICs. A study with similar aims on a full-column 3D sensor is given in [5]. Here a higher resolution study over a unit pixel cell in a double-sided 3D detector is presented. The detection response across a unit pixel cell to X-rays and high energy pions is mapped and the effects due to the columnar electrodes on the detection efficiency and charge sharing is investigated. The spectral response of the regions between the electrode columns, the full 3D region, and in the regions above and below the columns, the semi-3D region, are shown. This is studied through variations in the applied bias voltage and effective

2011 JINST 6 P05002

charge threshold used in the offline analysis. In the pion beam study the detection efficiency as a function of the angle of incidence of the pion beam to the surface of the sensor is measured. In the X-ray beam studies the charge sharing results are compared with a simple simulation. The double-sided 3D sensors tested and the readout ASIC used are discussed in the section below. The pion beam studies are reported in section 2 and the X-ray synchrotron measurements in section 3. The results from the two studies, and the relative advantages of the two techniques, are compared and overall conclusions are discussed in section 4. Further details of the telescope and the resolution results from this double-sided 3D detector are contained in the companion paper [6].

1.1 3D double sided sensors

The double-sided 3D sensor [7], as shown in figure 1(b), is a modification of the original design as first proposed by Parker et al. in 1997 [1]. This sensor configuration differs from that of single sided 3D sensors in that the columns do not traverse the entire depth of the sensor material, figure 1(b). This simplifies the fabrication process and increases the production yield. The difficulty of doping two different kinds of holes on the same side of the wafer is avoided. It is only necessary to create patterned electrode contacts on a single side of the wafer, the electrodes on the bottom side being shorted together. The double-sided 3D sensor has the advantage over full-column 3D sensors that all regions of the sensor have active silicon, as charge is still collected in the region above or below the columnar electrodes.

The devices investigated in this report were designed by the University of Glasgow and IMB-CNM and fabricated by IMB-CNM.[1] In this design inductively coupled plasma (ICP) is used to etch 10μm diameter holes to a depth of 250μm in a 285μm thick substrate sensor material figure 1(b). The high aspect ratio is made possible by an alternating sequence of etch and passivation cycles. p^+ and n^+ electrodes are produced by partially filling the holes with polysilicon and doping with boron and phosphorous. The junction is created at about 3μm into the silicon substrate as measured in a scanning electron microscope [7]. These measurements also show the polysilicon layer thickness is 3μm at each edge of the hole. This is passivated with an additional 1μm of silica. The sensor surface is passivated and the polysilicon at the electrodes is exposed and coated with aluminium to create the contacts for bump bonding to the readout chip.

Hole and electron collecting devices were fabricated. The devices used here are hole collecting double-sided 3D detector with n-type substrate and p-doped columns connected to the electronic readout. The devices were solder bump-bonded by VTT[2] to Timepix and Medipix2 readout chips. A lower grade readout chips were used for this R&D project with some inactive pixel columns (see section 1.2). The devices used here were fabricated from a wafer of resistivity 13kΩcm and had a leakage current of 3.8μA at 20V at room temperature.

The double-sided 3D sensor's depletion behaviour is more complex than that of the full-column 3D and planar designs. To test the depletion characteristics double-sided 3D pad sensors were fabricated consisting of 92 $\times$ 92 arrays of p-type readout columns with 55μm spacing, to match the pixel size of Medipix2. The 90 $\times$ 90 columns in the centre were connected by a metal layer to form a pad, and the surrounding ring of readout columns were connected together to form

[1] IMB-CNM, Centro Nacional de Microelectrónica. Campus Universidad Autónoma de Barcelona. 08193 Bellaterra (Barcelona), Spain.

[2] VTT Technical Research Centre of Finland, P.O. box 1000, FI-02044 VTT, Finland.

2011 JINST 6 P05002

a guard ring. During each test, the pad was held at ground, the back contact was biased, and a 10kHz AC signal was applied between the two. The result of one such test is shown in figure 3 of reference [8]. The capacitance decreases as the device depletes. A sharp drop in capacitance up to $\sim$2V occurs as the region between the columns depletes. The pixel region above the columns to the back plane depletes at a slower rate, with a depletion voltage around 10V, to ensure full depletion we operate at 20V.

1.2 Planar sensors

The planar sensors used were from a standard series of sensors produced by CANBERRA[3] for the Medipix2 collaboration. The substrates are n-type, and the devices have p+ electrodes for hole collection. The substrate resistivity was 32 kΩcm, corresponding to a 10V full depletion voltage for the 300μm thick device. The devices were solder bump-bonded by VTT to Timepix and Medipix2 readout chips.

1.3 Medipix2 and TimePix ASICs

Medipix2 and TimePix chips are readout ASICs produced by the Medipix2 collaboration for hybrid pixel detectors. The Medipix2 [9] and TimePix [10] chips each have 256 $\times$ 256 square pixels with 55μm pitch. Each pixel is independently coupled to the corresponding pixels of the sensor with an array of solder bump bonds. Together the sensor pixel and readout chip pixel form an independent readout channel. Each readout chip pixel contains amplification and digitisation circuitry.

Medipix2 is a photon counting chip; each pixel channel contains an amplifier, discriminator and 14 bit pseudorandom counter (giving up to 11,810 counts) that is iterated each time a signal from the sensor causes the amplifier signal to pass the discriminator's threshold. Timepix is a development of Medipix2 that adds the possibility to propagate a clock signal to each pixel to provide additional timing functionality. This clock signal can be used in conjunction with the counter to either precisely identify the time at which the signal arrived, or to measure the time the amplifier signal was over the threshold. These two modes Time of Arrival (ToA) and Time over Threshold (ToT) are programmable on an individual pixel by pixel basis in Timepix, along with the original Medipix2 counting mode. The ToT mode is used in the pion beam studies reported in this paper, where individual pions are tracked, as the triangular nature of the amplifier pulse means the time recorded is proportional to the amount of charge deposited in the pixel [10]. In the X-ray beam studies, where the pixel matrix is illuminated with a high photon flux, the counting mode of the Medipix2 chip is used.

To ensure that each pixel on the chip uses a similar threshold, both Medipix2 and Timepix pixels contain four bits of trimming information that can be individually programmed. The process of setting these values to provide a uniform global threshold is referred to as equalisation and compensates for small variations in the ASIC's fabrication. To set the global threshold for the chip a Digital to Analogue Converter (DAC) on the periphery of the chip provides a level that is adjustable in multiple electron steps, approximately 20-30 electrons per change of DAC least significant bit for the TimePix and Medipix2. The shaper and amplifier in the pixels are able to

[3]CANBERRA Industries, Semiconductor NV Belgium.

2011 JINST 6 P05002

operate in both positive and negative polarities allowing the system to collect either electrons or holes from n-type or p-type bulk sensors. Here only hole collecting sensors are reported.

The readout of Medipix2 and Timepix is performed by a shutter signal. When the shutter is 'open' the chip is sensitive and the counters are active, counting either the number of hits seen or the number of clock ticks where appropriate. When the shutter is closed the counters are reconfigured into 256 pixel long column shift registers and the data is read off as a matrix of values which are decoded by the readout system. The Medipix2, and TimePix assemblies in this paper, were readout using USB driven systems provided by CTU Prague [11] and the Pixelman data acquisition and control software [12]. These are the standard, portable, low bandwidth readout systems used in most Medipix applications to date. The USB1.1 readout system used was limited by the bandwidth of its link to the PC and could only sustain a frame rate of ∼2Hz. However in principle, each pixel can respond to an instantaneous particle rate of up to 1MHz [13].

2 Pion beam

2.1 Experimental set-up

A double-sided 3D n-type sensor, bump bonded to a TimePix readout chip, was tested in a high energy pion beam provided by the Super Proton Synchrotron (SPS) at CERN. The device was placed in the centre of a custom built telescope, as shown in figure 2. The telescope consisted of six detector planes, four TimePix and two Medipix2, each bonded to a standard planar 300μm p$^+$-*on*-n planar pixel device. The planes were separated from each other and the Device Under Test (DUT), by 78mm. This allowed the easy integration of the DUT, provided complete compatibility between the readout systems and enabled a track rate of 200Hz. The hit position in each TimePix station was obtained from a weighted centroid of the time-over-threshold for the hit pixels. As the Medipix2 planes only provide binary information, and so produce a lower resolution, they were placed in the least sensitive positions with the TimePix assemblies forming the inner and outermost stations of the telescope arms. The telescope planes were angled at 9^o in both the horizontal and vertical axes perpendicular to the beam line. This angle produces multi-hit cluster and is close to the optimal point of the spatial resolution, which lies at an angle of approximately $\tan^{-1}$(pitch/thickness), that could be achieved by the telescope. The DUT was mounted at the centre of a symmetric arrangement of chips to further increase the resolution that could be achieved. Further information on the telescope performance can be found in [6]. A standard planar TimePix detector, as used in the telescope planes, was also tested as the DUT allowing a direct comparison with the double-sided 3D detector to be made.

To investigate the efficiency of the 3D device at different angles, the DUT was mounted on high precision rotation and translation stages driven by stepper motors that allowed it to be turned and aligned remotely. The stages had 2μm and 50μrad precision for the translational and rotational motion respectively.

The absolute DAC value at which the applied threshold corresponds to the pedestal of the pixel varies between individual chips due to slight fabrication differences. The DAC controlling the global threshold, THL, is set with respect to the mean of the distribution of equalised noise edges. The absolute values were set to give a threshold of approximately 1600 electrons in the assemblies that made up the telescope and in the DUTs.

2011 JINST 6 P05002

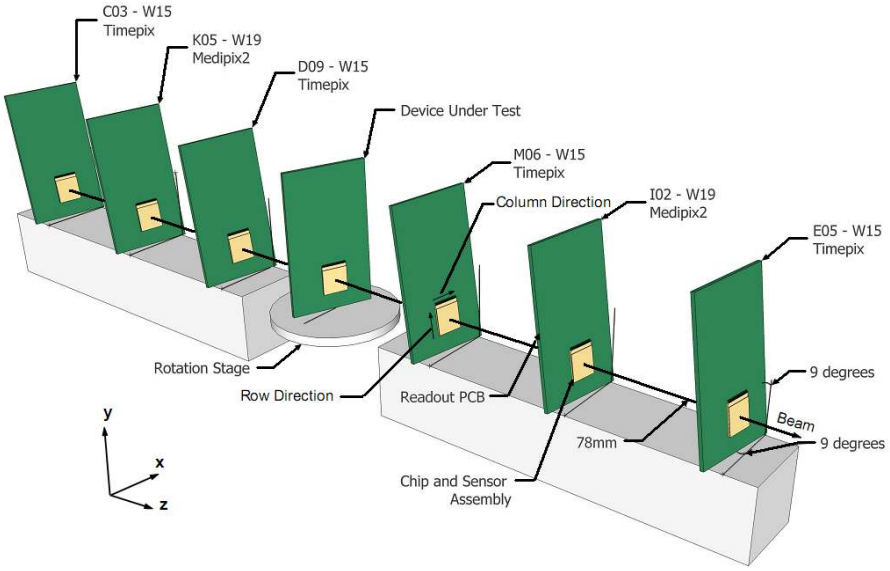

Figure 2. A diagram of the pixel detector assemblies within the telescope, showing the angled four TimePix and two Medipix2 detectors and the TimePix DUT with its axis of rotation.

A trigger signal is applied simultaneously to all the USB readout units and its rising edge triggers local shutters of individual chips. The length of the shutter was set to be the same for each assembly. It was optimised on a run-by-run basis, depending on beam conditions, to capture between 100 and 500 tracks per frame. The microcontroller in the USB unit readout produces a delay between the trigger being received and the shutter being sent of $4\pm0.5\mu$s. The minimum shutter periods used in this study were 10ms. The error on the measured efficiency due to reconstructed tracks arriving outside the active shutter period of the DUT is negligible.

2.2 Analysis and track reconstruction

The cluster finding, track reconstruction and alignment procedure are reported in detail in [6], a brief summary is provided here.

A cluster is obtained from joining all adjacent hit pixels. The position of the cluster is determined from a charge weighted average of the contributing pixel positions in the row and column directions. A minimum and maximum cluster charge cut is applied for the clusters in the tracking.

A simple pattern recognition algorithm is applied to identify the clusters on tracks. A global event cut of 5000 hits is used to remove a small number of saturated events. Taking a central detector as a primary reference plane each plane within the telescope is examined in turn. A set of clusters on each telescope plane that are within $\pm100\mu$m of each other are then identified. A cluster is required on all planes in the telescope. A straight line track fit is then applied using the full alignment information.

A software alignment was performed using an iterative procedure by minimising the residual between the track intercept position and the reconstructed cluster position. All degrees of freedom were aligned, the displacement of each plane in the row and column directions and along the beam, and the rotation of the planes around all three axes. The same procedure was applied to the DUT.

2011 JINST 6 P05002

After alignment the residual means were centred on zero, and the variation of the mean of the residual across the width of the detector was below $\pm 1\mu$m. The distribution of the biased residuals has been studied to extract the resolution of the individual telescope planes and the precision of the track intercept point at the DUT. The resolution at the DUT in both the column and row directions is found to be $2.3 \pm 0.1\mu$m

A number of additional cuts were applied to select a 'clean' data sample. First, the centre of clusters considered in the analysis of the DUT were required to be within 200μm of the track intercept point. In addition, all tracks considered in the analysis were required to be separated by more than 600μm at the DUT.

The Timepix chip used for this R&D project with the 3D sensor was of a lower grade and had two non-responding columns (512 pixels). Furthermore, the bump bonding of the sensor was not perfect and introduced some further dead or noisy pixels. A map of dead and noisy pixels was produced exposing the sensor for 20 minutes to an X-ray source. An average of 1000 counts was obtained per pixel, and those pixels more than four standard deviations from the mean were flagged as dead or noisy. This identified an additional 128 pixels, which were excluded from the analysis. This map was used in the analysis and all extrapolated tracks within 3 pixels of a dead or noisy pixel on the 3D sensor were excluded from the analysis. Furthermore, all extrapolated tracks were required to be more than 7 pixels from the edge of the 3D sensor.

The ToT counts in the TimePix are not linearly related to the charge deposited for low values of charge [14]. At higher levels of deposited charge the relation is linear but with an offset in each pixel. Hence the effect of a ToT cut on one pixel and multiple pixel clusters differs. This is described in detail in [6], where a calibration procedure is described. Hence, in this paper we specify in each case whether ToT cuts are applied to the cluster or a single pixel.

The detector was positioned approximately perpendicular to the beam and the alignment was determined by minimising the ratio of the average number of pixels in the columns direction of the sensor contributing to a cluster to the same quantity in the row direction, and by maximising the fraction of single pixel clusters [6]. The detector is rotated around the vertical axis during the studies reported here. The sensor is estimated to be offset from the set angle of rotation by -0.3^o. The following plots are labeled with the rotation angle set, rather than the true angle, of the sensor. This alignment accuracy corresponds to a lateral deviation of the beam by 1.6μm as a track travels through the full thickness of the sensor substrate. This is less then the nominal diameter of the columnar electrode of 10μm, but adds an additional smearing to the results.

2.3 Landau distributions

Particle tracks reconstructed by the telescope are used to find the track intercept positions on the DUT. The energy deposited in the pixel on the DUT where the track intercepts is obtained by operating the TimePix in ToT mode. Figure 3 shows the mean energy deposited by a particle as a function of the track intercept position inside a pixel cell. The results from the full sensor have been mapped onto a single pixel. Figure 3(c) shows the mean energy deposited in the hit pixel while figure 3(f) shows the mean energy of the cluster, combining the charge deposited in the hit pixel with that of its neighbours. The frequency of the collected number of ToT counts for areas of interest are shown in figures 3(a), (b), (d) and (e).

2011 JINST 6 P05002

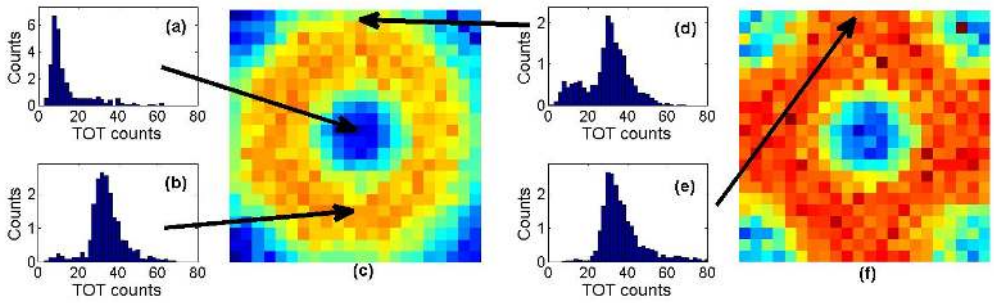

Figure 3. Histograms of the ToT counts in the central electrode region (a), away from the central electrode and pixel edges (b). Pixel maps showing the mean energy deposition across the pixel matrix, for a single pixel (c) and the energy in clusters (f). (d) and (e) show the histograms of the energy deposited at the pixel edges for the single pixel and the clusters.

In the area away from the collecting electrodes and the pixel boundary, the energy response, figure 3(b), exhibits the standard Landau shape expected from MIP detection. In the area of the central electrode the average recorded energy reduces as shown in figure 3(a), a similar distribution was also seen for the corner electrodes. This is interpreted as no charge being collected in the electrode column but charge being collected in the semi-3D region of the 35μm silicon above the central electrode. The ToT value is not linearly related to the charge deposited but can be corrected for with a calibration curve. After applying the appropriate calibration curve values from [6], a ratio of the most probable value of the Landau distribution in the region above the electrode and the region away from the electrodes of 11$\pm$3% is obtained. This is in agreement with the expected ratio of 12% from the height of the region above the central electrode (35μm) to the full device thickness (285μm).

The ToT value measured at track intercept positions along the boundaries of the pixel, but away from the corners, is shown in figure 3(d). A number of counts at lower energy deposition than in the main peak is observed, which is expected due to charge sharing with the neighbouring pixel. If the charge deposited in the neighbouring pixels is combined into the cluster charge, figure 3(f), then the full energy Landau shape is resolved at the pixel edges figure 3(e). The charge sharing is discussed in further detail in section 2.7.

2.4 Efficiency distributions at normal incidence

The efficiency for having a reconstructed cluster position within $\pm$200μm of the track intercept position is evaluated. The efficiency maps are projected onto a unit pixel cell with entries placed at the track intercept point. Samples of approximately 30,000 particles recorded in the telescope were used. Bias voltages of 2V, which depletes the region between the columns, and 20V, which fully depletes the sensor, were studied. Errors for all efficiency measurements are calculated from the probability of associating a noise hit to the track position and found to be $\leq$0.5%.

Figure 4 shows the efficiency measured across the pixel for 2V and 20V bias. To probe the efficiencies of the different pixel areas we define three regions. The central electrode region is defined as a 5μm radius circular region centered on the central electrode. The corner electrodes region consists of quarter circle areas of the same radius in the pixel corners. A 5μm radius has

2011 JINST 6 P05002

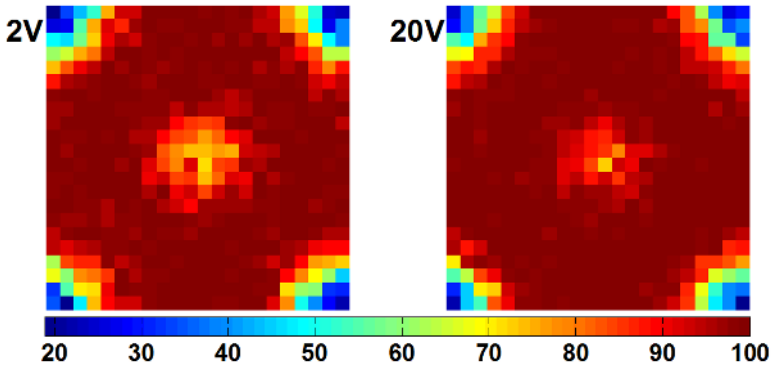

Figure 4. Pixel efficiency maps at normal incidence to the pion beam with the sensor biased at 2V and 20V.

been chosen here as this corresponds to the size of the etched electrode. A third region defined is the area of high counts, away from the electrode regions. This is defined as the area outside a 15μm radius region from the corner and centre electrodes. A 15μm radius has been chosen as this excludes all potential for reduced counts due to the electrode column size, 5μm radius, the diffusion of the dopant into the substrate of 3μm around the polysilicon layer [7], the smearing of the low count region by the resolution of the telescope, 2.3μm [6], and the sensor being not quite perpendicular to the beam.

For normal incidence tracks with a 20V bias voltage applied the overall efficiency of the pixel is 93%, with a clear drop in efficiency evident at the positions of the electrodes. In the region away from the electrodes an efficiency of >99% is already measured at only 2V.

At 20V bias an efficiency of 86.7% is found in the 5μm radius region around the central electrode. Particles incident on this region deposit charge in the 35μm of the depleted substrate above the columnar electrodes. The efficiency in this region is still reasonably high in this double-sided 3D sensor, in contrast to that in a single-sided 3D sensor [5] as the ~2800 electron-hole pairs typically deposited in 35μm is greater than the detector threshold of approximately 1600 electrons. A larger drop in efficiency is observed around the corner electrodes where an efficiency of 35.6% is measured at 20V bias. Particles incident on the corner electrodes will also travel through 35μm of depleted Si at the columns. However charge deposited at the corners will be shared by up to four pixels, and each portion of the charge collected by an individual pixel may fall below threshold. At 2V the corner and centre efficiencies both drop compared with 20V. This is to be expected as the region above/below the electrodes is less depleted at 2V. In the 20V biased data applying a cut on the charge of the pixel cluster at a ToT level of 20 (around 13k electrons) requires that particles have deposited charge in the full 3D region, not just the region above/below the electrodes (c.f. the Landau distributions above). As expected this causes the efficiency values at the centre and corner of the pixel to reduce significantly.

The efficiencies measured around the centre and corners can be interpreted as effective insensitive column sizes. The efficiency is calculated in a 15μm radius region around the electrode columns, an area containing the full region with reduced efficiency due to the electrodes. This region is then modeled as an inefficient column surrounded by a fully efficient area. The radius

2011 JINST 6 P05002

Table 1. Efficiencies of different regions of the pixel (see text for definitions) with 2V and 20V bias applied measured in the Pion beam.

	Efficiencies (%)			
Voltage	Corner	Centre	Area of high counts	Pixel
2V	35.6 ± 0.5	79.1 ± 0.5	99.1 ± 0.5	91.2 ± 0.5
20V	39.1 ± 0.5	86.7 ± 0.5	99.7 ± 0.5	93.0 ± 0.5
20V 20ToT cut	18.8 ± 0.5	14.2 ± 0.5	98.1 ± 0.5	78.9 ± 0.5

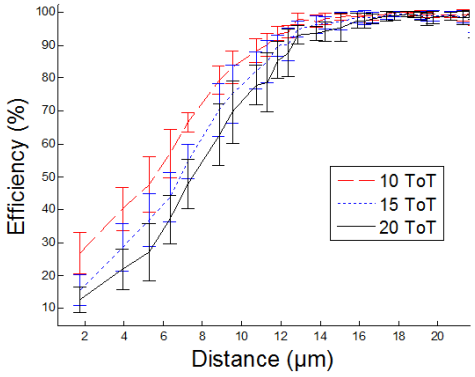

Figure 5. Average efficiencies of the 20V pixel map at different threshold cuts plotted against the distance from the centre of the pixel.

of the column required to obtain the measured efficiency in this region is calculated. At 20V bias, applying this calculation to the central electrode results in an insensitive column radius of only 2.7μm. This result is smaller than the true electrode column size since charge is collected in the region above the central electrode. Applying a ToT cut of 10 to 20 counts on the charge of the pixel cluster removes the charge collected above the central electrode, and gives an effective radius corresponding to the column in the full 3D region of the device of $7.5\pm0.8\mu$m. This is compatible with the known column dimensions and dopant diffusion. The corner regions, which may tend to overestimate the size due to additional charge sharing effects, give an effective radius of $8.7\pm1.3\mu$m.

An alternative measurement of the size of the inefficient region around the central electrode is obtained from plotting the efficiencies as a function of their distance to the pixel centre, as shown in figure 5. A threshold cut is applied to the total pixel cluster charge between 10 and 20 ToT, to remove the charge collected only in the Si volume above the column. The line connects the average efficiencies at each position and the error is given by the standard deviation between values obtained for regions at this distance. The FWHM gives a value of $7.6\pm0.6\mu$m, where the error is assigned from varying the ToT cut. This is in line with the expected etched column size and dopant diffusion and with the value obtained from the first method above.

2011 JINST 6 P05002

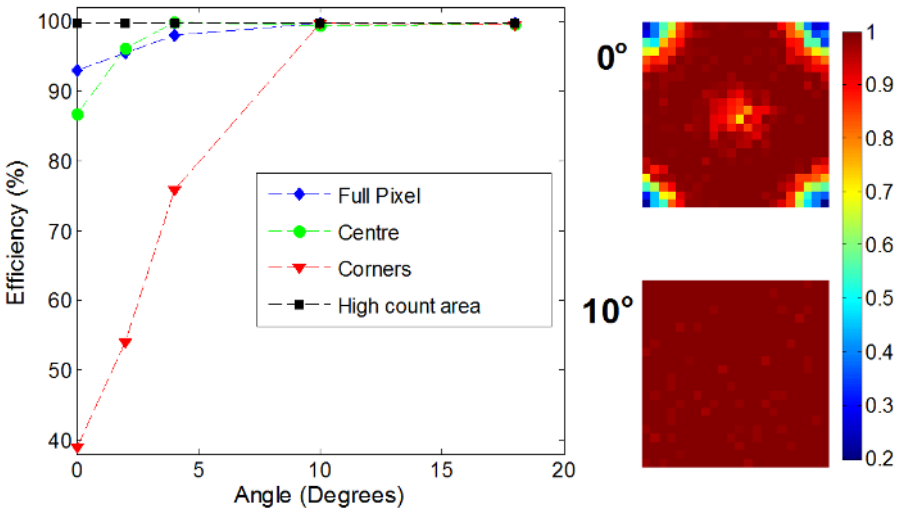

Figure 6. Efficiencies in regions of the pixel (see text) as a function of rotation angle. Also shown are pixel maps of the efficiencies at 0^o and 10^o showing the fully efficient response at 10^o across the entire pixel.

2.5 Efficiency distributions at angles

The efficiency map study was repeated with the DUT rotated by up to 18^o around the vertical axis. In figure 6 the efficiencies of selected regions of the detector are shown. The corner, centre and high count regions are defined as in section 2.3. As the angle is increased a track traverses less of the electrode column and a greater section of the depleted Si. At 10^o and higher the electrodes have no effect on the efficiency measurements and an efficiency of 99.8±0.5% is reached across the pixel matrix. At an angle of 10^o the track traverses a full pixel within the thickness of the sensors, as shown in [6] this is the angle of best resolution.

2.6 Single pixel efficiency versus threshold

Applying energy threshold cuts on the 3D and planar devices further illustrates the difference between the devices and their spectral responses. The track is intercepted with the DUT and the single pixel efficiency of finding a hit in the intercepted pixel is obtained. Here the efficiencies measured are lower than those reported in section 2.4 when clusters (multiple pixel efficiencies) are recorded. Figure 7 shows this single pixel efficiency for regions of the pixels plotted against a ToT threshold value cut that was applied offline to the collected data. The same region definitions as introduced at the start of section 2.3 are used.

As discussed above, an increase in the energy threshold set across the 3D device removes the low energy counts that are deposited in the Si above the central column. Threshold cuts at this level also remove the charge deposited at the corners where particles shared energy with the neighbouring pixels. As the thresholds increases the single planar device efficiency is also affected by losses at the pixel corners and edges due to the high level of charge sharing in the planar device. There is a relative scaling factor of four between the ToT counts on the planar and 3D detector as a result of different clock speeds being used. The full scale range of ToT cut values used on the plot (0–35) for the 3D sensor corresponds to roughly 1.6k to 26k electrons.

2011 JINST 6 P05002

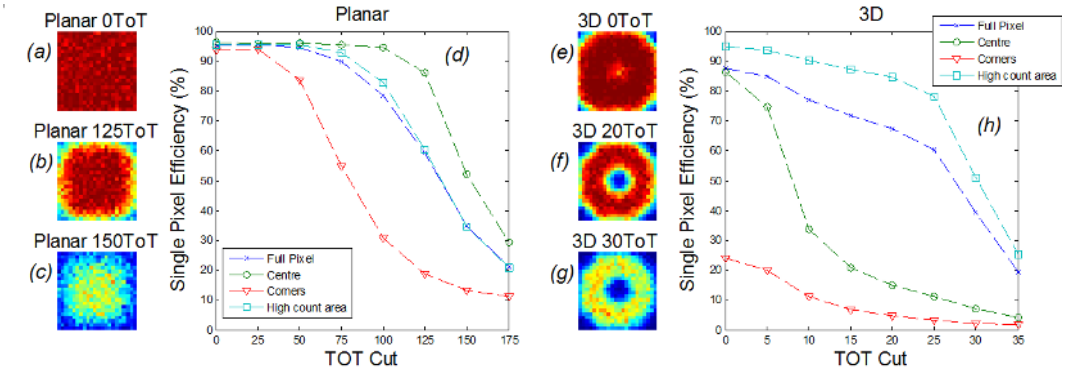

Figure 7. Single pixel efficiency maps for the 3D devices and the planar sensor at different threshold settings illustrating the regions of the loss of counts at high threshold values. The graphs give numerical values for the efficiency values in the different regions. (a)-(d) are for Planar pixels with (e)-(h) for 3D pixels.

2.7 Charge sharing

As briefly discussed in the introduction, in the 3D device charge drifts towards the collecting electrode at the centre of each pixel cell. This contrasts with a planar device in which the charge is drifted through the device thickness, which permits diffusion of the charge across pixel cell boundaries and leads to charge sharing. Figure 8 shows the positions of the track intercepts of the particles mapped onto a unit pixel cell in the detectors. Single pixel hits, hits creating clusters of two pixels and clusters containing three or more pixels are plotted separately. Both sensors were operated above full depletion, with the 3D sensor biased to 20V and the planar sensor at 100V. Single pixel hits in the 3D device can be found to be spread across almost the entire pixel, figure 8(a), with a slight reduction at the pixel edge and corners. In comparison the single hits in the planar device are confined to the central section of the pixel. Particles incident outside the central pixel area share their created charge with two (f) or more (g) pixels. This is best illustrated by the ratio of multiple hit clusters to single pixel hits for the 3D (d) and planar (h) devices. 59% of incident particles share sufficient charge with neighboring pixels to create multiple pixel hits in the planar detector. This is compared with 14% in the 3D device. Hits along the boundary of two pixels create double hit clusters as expected in both devices. Hits in three or more pixels are seen at the corners of the pixels in the planar device. These are not evident in the 3D device due to the additional loss of charge in the corner electrodes.

Track position maps for tracks of 10^o incidence angle, rotated around the vertical axis, are shown in figure 9. Broadly speaking the one pixel clusters occupy the central region and the two pixel clusters the left and right-hand regions as expected. The reduced charge sharing in the 3D detector compared with the planar detector is again evident in comparing the one pixel clusters. The 3D detector single pixel cluster region widens at the upper and lower parts of the figure, as charge is lost to the corner electrodes in the neighbouring cells at these positions. In the two pixel clusters, the increased charge sharing in the planar detector is shown by the regions at the top and bottom where charge is spread to more than two pixels, which is not seen in the 3D detector.

2011 JINST 6 P05002

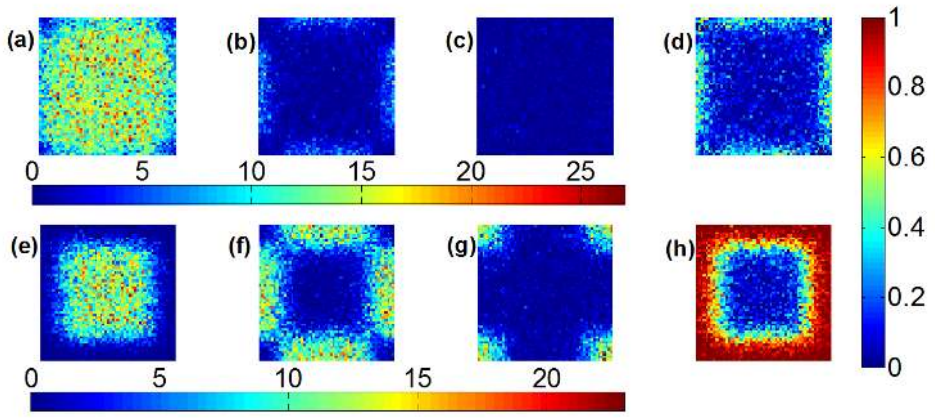

Figure 8. Track intercept positions across the 3D pixel matrix in a single pixel cell for tracks of normal incidence, for one pixel clusters (a), for two pixels clusters (b), for clusters sizes >2 (c). The ratio of (hits>1)/(total hits) (d). Track positions across the planar pixel matrix, for one pixel clusters (e), for two pixels clusters (f), for clusters sizes >2 (g). The ratio of (hits>1)/(total hits) (h). Values in (a)-(c) and (e)-(g) are in numbers of counts.

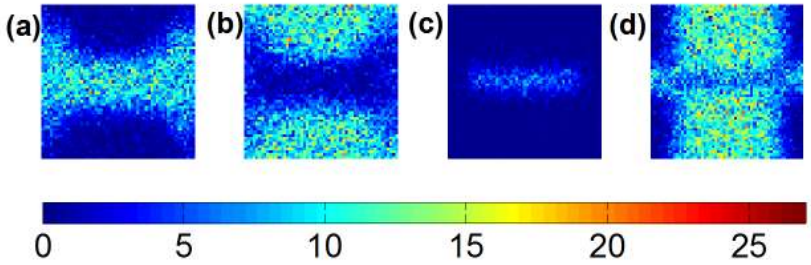

Figure 9. Track positions across a unit pixel cell for tracks of 10^o incidence, for one pixel clusters in 3D detector (a), for two pixel clusters in 3D detector (b), for one pixel clusters in the planar detector (c), for two pixel clusters in the planar detector (d). Values in number of counts.

2.8 Conclusions

The detector response to a high energy pion beam has been mapped across a unit pixel cell. Efficiency measurements show a pixel efficiency of $93.0 \pm 0.5\%$ at normal incidence. The efficiency loss in the pixel is shown to be due to loss of charge in the region of the electrode columns. The effective inactive column radius is estimated as $7.6 \pm 0.6 \mu$m, in good agreement with the scanning electron microscope measurement of the junction position [7]. However, charge collection in the regions above and below the electrode columns is still observed, and shown to improve as the bias voltage is increased and this region becomes further depleted.

By tilting the angle of the detector by 10^o relative to the particle beam the influence of the columns become negligible on the detector efficiency. A full pixel efficiency of $99.8 \pm 0.5\%$ is reached across the unit pixel. For future high energy physics experiments we would recommend careful consideration of the layout to arrange the detectors such that the angle of incidence of the particles of interest is around 10^o or greater. This consideration couples well with the requirement

2011 JINST 6 P05002

to arrange the silicon for minimum Lorentz angle and to achieve overlap with a multi-module system in a barrel system, and may match the angular acceptance of forward endcaps in some systems.

The different behaviour of the central, corner and main areas of the pixel are distinguished by mapping the energy deposition information available from the ToT mode of the TimePix readout ASIC. The reduced level of charge deposited above the central electrode is observed to be compatible with being from the expected 35μm height of silicon in this region.

The effect of the electric field within the 3D sensor in reducing the charge shared is illustrated by mapping the ratio of multiple-hit clusters to single-pixel hits. This reduces the spatial resolution of the system at normal incidence, since charge sharing in an analogue readout system increases the chance of creating multiple-hit clusters from which a weighted centroid position can be determined. However, a decrease in the level of charge sharing may be advantageous for highly irradiated detectors which suffer from low signal-to-noise ratios as this ratio is improved by collecting all the signal in a single pixel.

3 X-ray synchrotron radiation

3.1 Experimental set-up

A micro-focused X-ray beam was used to probe the 3D detector response across a single pixel and compare it to that of the planar device. The set-up is shown in figure 10. The micro-focused beam was provided by the B16 beamline at the Diamond Light Source synchrotron research facility. This beamline comprises of a water-cooled fixed-exit double crystal monochromator that is capable of providing monochromatic beams over a 2-20keV photon energy range. An unfocused monochromatic beam is provided to the experimental hutch. A compound refractive lens (CRL) was used to produce a 14.5keV micro-focused X-ray beam. This energy is within the region of energies typically used for macromolecular crystallography.

The size of the micro-focused beam was measured by measuring transmissions scans with a 200μm gold wire. The derivative of these scans gave FWHM of 4.5$\pm$0.3μm and 6.7$\pm$0.3μm in the vertical and the horizontal directions respectively. The beam divergence at the micro-focus position is calculated as 0.26mrad. Line scans were performed at the start and end of the experimental run and no variation in the beam size was measured within the stated errors.

The DUT was mounted on precision translational and rotational stages giving all six degrees of freedom, figure 10. The translational and rotational stages had 0.1μm and 5μrad precision respectively. As with the high energy testbeam the USB interface [11] and Pixelman software [12] was used to connect and control the chip. The detectors were operated in Medipix counting mode. The typical shutter time of 70ms was used to obtain approximately 5,000 hits in the target pixel.

The detector movement was automated so that the micro-focused beam was made to raster scan a square area of 77.5μm sides, centered on a 'target' pixel, as illustrated in figure 10. The detector was moved in steps of 2.5μm. Maps of the detector response across a unit pixel cell were generated by combining the images taken at each scan position.

The X-rays deposit their energy throughout the thickness of the sensor with 50% of 14.5keV X-rays depositing their energy within 285μm of Si. However, it does probe the front-surface of the sensor more than the back: the 35μm region above the central electrode (which faced the beam)

2011 JINST 6 P05002

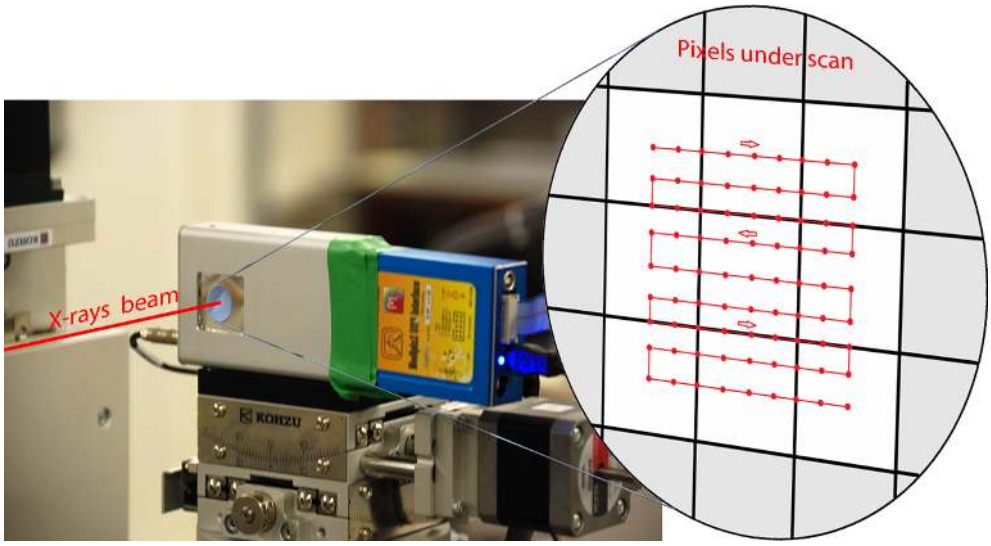

Figure 10. Detector in its housing box with readout card, mounted on the motorized stages. The inset schematic illustrates the principle of the raster scan.

has 9.2% of X-rays depositing their energy, while the 35μm region below the corner electrodes absorbs the interactions of only 4.4% of X-rays.

3.2 Alignment procedure

The detector was aligned perpendicularly to the incoming radiation, α=90^o. This was performed by rotating the DUT through a large angle, β (typically $\sim$45^o) either side of the angle of investigation, α. At a given rotation angle β around the vertical axis, the detector was positioned such that the beam intercepted a pixel on one edge of the device. The device was then moved horizontally on the stage by a distance, D, so that the beam intercepted the device close to the opposite edge of the pixel matrix. The measurement was repeated at an angle -β moving the detector so that the image moved by the same number of pixels. The difference ΔD in the distance D to move the image the same number of pixels across the pixel matrix can be used to find the correction angle θ such that $\theta = 90^o$-α

$$\theta = \tan^{-1}\left(\frac{\Delta D}{2D \cdot \tan\beta}\right), \tag{3.1}$$

After a number of iterations the correction angle θ was minimised to 0^o within error. The process was repeated for vertical movements of the stage. The accuracy of the measurement was found by error propagation due to the uncertainty of a single pixel measurement on D. The error in the accuracy of the stage movement was negligible. The uncertainty was compared with the rms of multiple calculations of θ. Both methods were in excellent agreement and an accuracy of 0.3^o and 0.9^o in the horizontal (x) and vertical (y) directions respectively were obtained. The larger error in the y direction is due to the limited movement of the stage that restricted β when rotating around the horizontal axis. The alignment accuracy corresponds to a lateral deviation of the beam by 2μm (horizontal) and 5μm (vertical) as the beam travels through the full thickness of the sensor substrate. This is less then the nominal diameter of the etched columnar electrode, 10μm, but will affect the charge collected in the region around the electrode.

2011 JINST 6 P05002

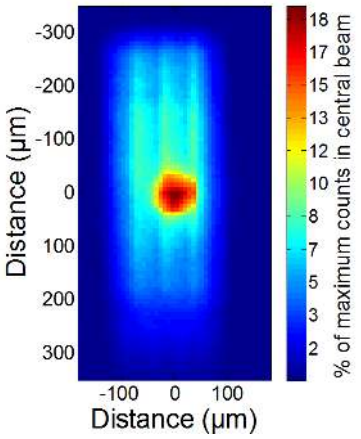

Figure 11. A map of the background created by recording the responses of a number of pixels surrounding the micro-focused beam for the 3D detector. The color scale shows the values as a percentage of the maximum counts from the central micro-focused beam.

3.3 Background analysis

The micro-focused beam was seen to have a widely spread background beam of lower intensity, with a peak height of approximately 18% of the micro-focused beam. The origin of the background beam is unknown but may be due to a combination of X-ray fluorescence and higher order harmonics within the beam which may not have been focused by the CRL. X-ray fluorescence is present from metals in the chip, the bump bonds and the printed circuit board. To create a profile of the beam background a large number of images where the micro-focused beam was close to the central region of the target pixel were analysed. In these images the counts observed in the neighbouring pixels will not be affected by charge sharing but are due to the beam background. A map was built up of the beam profile showing the response of the target pixel to the micro-focused beam and the neighbouring pixels to the background beam. This map was fitted with splines in both the x and y direction at each measured position, so that the effect of the beam background on the central pixel was found. The resulting background map is shown in figure 11. The profile of the beam background was found to be highly asymmetric and spread over a much larger region than the micro-focused beam, having a $\sim$200μm FWHM. The map of beam background counts was subtracted from the pixel maps shown in the following sections.

3.4 Efficiency maps

The number of counts in the target and surrounding pixels was measured as a function of the detector position relative to the beam and background subtracted. The current in the synchrotron was monitored and no significant variation in the incident beam flux is expected during the measurement scans. The number of incident photons is not known so an absolute measure of efficiency cannot be produced. Instead the total number of counts observed was normalized to 100% efficiency in a region of known high efficiency. The region away from the central and corner electrodes, measured to have an efficiency of 99.7% in the pion testbeam analysis in section 2.3, was selected and the average of this area was chosen as the fully efficient count rate.

2011 JINST 6 P05002

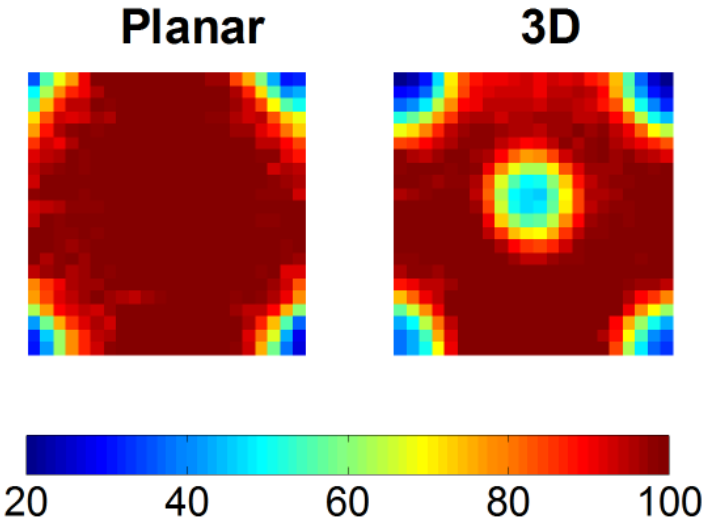

Figure 12. 55μm pixel efficiency maps normalized to the average number of counts in fully efficient area as explained in the text.

Table 2. Efficiencies of different regions of the pixel (see text for definitions) with 20V bias applied measured with X-rays.

	Central Electrode (%)	Corners (%)
Planar (100V)	102 ± 3	43 ± 12
3D n-type (20V)	51 ± 5	35 ± 9

The map of normalized efficiency as a function of the micro-focused beam position is shown in figure 12, and numerical results in different regions are given in table 2. The selected regions of table 2 are as defined at the start of section 2.3. The uncertainties on the efficiencies in table 2 are obtained from the rms variation of the measured values for the scan points in these areas. The full 77.5μm scans are cropped to show maps of a single pixel in figure 12. The 3D sensor was biased to 20V and the planar sensor to 100V. The numbers of counts in the normalized efficiency maps are the sum of the responses of the nine pixels centred on the target pixel. This sum of counts is taken as photons incident on the pixel boundary may count in either of the two pixels. The threshold level for counts to be registered in the ASIC was set at approximately 50% of the incoming X-ray energy, approximately 2000 electrons. This threshold was chosen as it is the typical value set in imaging applications since it minimizes the effect of charge sharing at the boundary of two pixels. In comparison the threshold level set for the pion experiment was set close to the noise floor where cluster analysis is employed.

The 3D detector shows a reduced number of counts at scan positions close to the central electrode and both detectors show a reduction at the corners of the pixel. In the planar detector, the drop in normalized efficiency to 35% at the corners is due to charge sharing. The charge cloud created by X-ray interactions in this region is likely to be shared between three or four pixels which

2011 JINST 6 P05002

reduces the charge collected in each individual pixel below the threshold value and hence no count is registered. A similar drop in efficiency, to 43%, is seen at the corners of the 3D sensors but this is primarily for a different reason. The 3D detector has less charge sharing than the planar detectors but a reduced number of counts is registered due to the presence of the electrode columns in the sensor substrate. The corner regions in the 3D detector map have the shape of quarter sectors of a circle due to the cylindrical shape of the electrode. In the planar device these regions have a more triangular shape.

Overall, assuming the central region used for normalisation to be fully efficient, the 3D detector has an efficiency of 90% and the planar detector 95%. The same methodology as in section 2.3 is applied to determine an effective inefficient column size from the region around the central electrode in the 3D sensor. This gives an estimate of a 6μm radius column.

3.5 Charge sharing

As demonstrated in section 2.4 and in the author's previous synchrotron study [15], the 3D detector has reduced charge sharing compared to the planar detector. Charge shared between neighbouring pixels can result in the loss of counts as is evident in the corners of the pixels in the efficiency maps in figure 12. At low threshold settings the sharing of charge across pixel boundaries can result in double-counting and similarly under-counting at high threshold settings. The amount of over-counting and under-counting at the border of two pixels at low and high threshold values is an indication of the level of charge sharing. Figure 13(a)–(c) and (d)–(f) show the corner of a scanned planar and 3D pixel respectively at three different threshold settings, named low, medium and high thresholds. Calibrations of the threshold level were performed using the X-ray fluorescent lines, $K\alpha_1$ of Ni the $K\alpha_1$ of Mo and the micro-focused beam energy. Energy levels of approximately 4keV are set for the low thresholds on the 3D and planar devices which corresponds to approximately 1100 electrons. This is approximately 100 electrons above the expected minimum detectable energy of the chip, 3.6keV. A medium threshold level corresponds to approximately half the beam energy and high threshold levels are set to approximately 11keV, 3000 electrons, for both devices. Regions along the pixel boundaries in the planar device can be seen to double count (a) and under-count (c). In figure 13(b) there is little evidence of charge sharing along the pixel edge where the count is in one pixel or its neighbour. However at the pixel corners charge spread between more than two pixels leads to a reduced number of counts. Similar behavior can be seen in the figure 13(d)–(f) for the 3D pixels. Here the same regions of under- and over-counting can be seen but in addition areas of lower counts occur at the electrode positions.

Considering the variation in counts across the border between neighbouring pixels provides an indication of the level of charge sharing. The average number of counts observed as the beam is scanned across a pixel boundary was plotted. The region of the scan used is indicated by the black box in figure 13(f). These line scans are normalised to the average number of counts measured when the medium threshold level is set. The line scans are shown in figure 13(g)–(h) for both sensor architectures at the three different threshold settings. At medium threshold setting both sensors show a flat response as expected. A decrease in the amount of under and over-counting is evident at the other thresholds: for the planar device approximately one in every two photons at the pixel boundary is double counted at low thresholds or lost at high thresholds; this occurs for less than one in three photons for the 3D detector at the boundary. The distance into the pixel in

2011 JINST 6 P05002

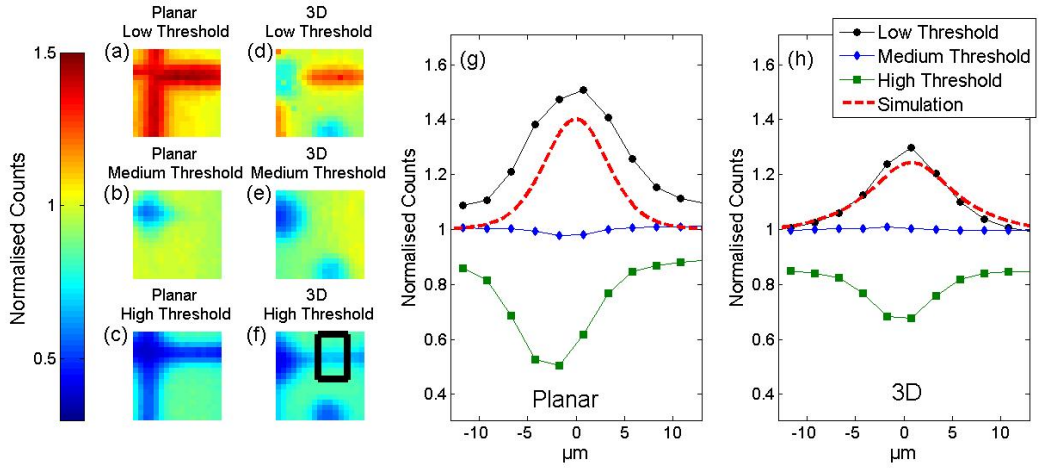

Figure 13. Maps of a 42.5μm square region showing the top corner of a pixel in both the planar and 3D devices with (a)+(d) low, (b)+(e) medium and (c)+(f) high threshold settings. The number of counts in each of the maps is normalised to the average number of counts in the medium threshold maps. Normalised line scans across a 25μm region for the planar (g) detector and 3D detector (h).

which charge sharing has an effect is also larger in the planar detector: the FWHM of the curves are approximately 12μm and 8μm for the planar and the 3D device respectively. Combining these effects 60% less photons share their charge between the pixels in the 3D detector at this boundary.

The lower baseline number of counts in the devices in figure 13 at the higher threshold setting can potentially be explained by the presence of a background of X-ray fluorescence. This may be emitted from metals present in the bump bonds, the read-out ASIC and the printed circuit board: Au, Ag, Pb, Sn, Ni and Cu all have X-ray fluorescence lines between 7.5keV and 14.5keV. It has been shown that background fluorescence from these materials can lead to counts in the device itself [16]. Hence, at high threshold we may remove some of the background counts originating from these materials that are present in the scans with lower threshold levels set. In addition, at a threshold of approximately 11keV counts may be lost from the lower energy tail of the 14.5keV photopeak, this effect is not expected to be large as the FWHM of a Medipix2 has been measured as approximately 2.4keV [15].

A simulation of a simple model of charge sharing for the low threshold setting was performed using Monte Carlo N-Particle Transport code MCNP [17]. Figure 14(a) shows the average energy deposition as a function of position simulated for 10^6 15keV photons in Si incident on a point on the sensor surface. The charge is projected onto the sensor surface and normalised in figure (b). Diffusion of the charge cloud inside the planar sensor can be described by a Gaussian function of width, $\sigma = \sqrt{(2kTd^2/\mathrm{qV})}$ [18], where d is the distance over which the charge cloud is collected, T is the temperature, V the applied bias voltage, k is the Boltzmann constant and q is the charge of an electron. The diffusion spreading function, figure 14(b), is a weighted average of these Gaussian spreading distributions. The weighting factors are given by the depth of the interaction which is calculated from the linear attenuation coefficient. The convolution of the diffusion function and the average deposited energy gives the average collected charge as shown in figure 14(c). Sufficient energy must be collected by a neighbouring pixel to allow double counting, hence a distance to

2011 JINST 6 P05002

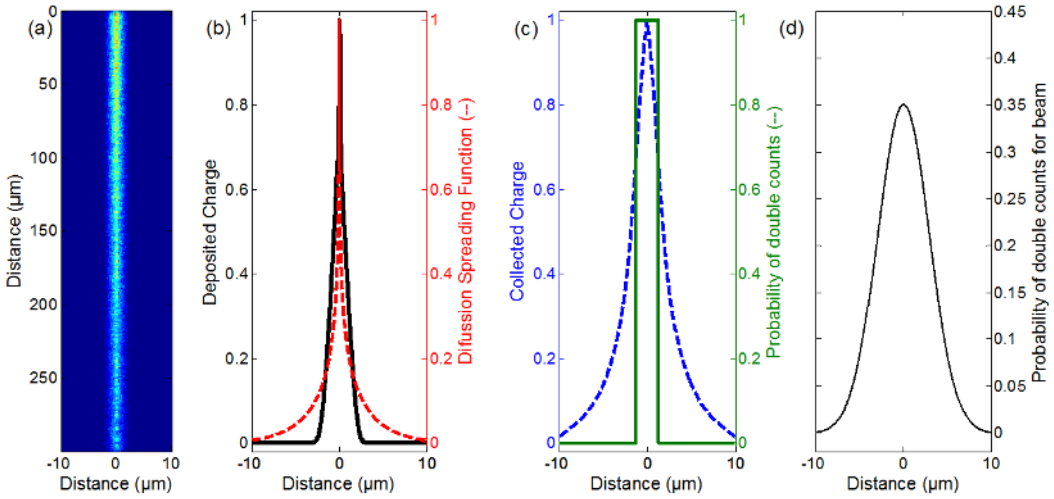

Figure 14. (a) Average charge deposition in 300μm thick silicon, (b) the normalised deposited charge and the diffusion spreading function, (c) the normalised collected charge and the probability of double counts for the 'average photon'. (d) The simulated probability of double counts for a 15keV beam of FWHM 6.7μm, note this does not include the background beam energies.

the pixel edge inside which double counting will occur can be obtained from the collected energy distribution, as shown in the probability of double counts in figure 14(c). By convoluting this average photon response with the beam profile the probability of double counts in a planar device is estimated, figure 14(d). The background, which we believe to contain fluorescence X-rays and also higher order harmonics from the beam, is simulated in the same manner. A value of 45keV is taken for the higher harmonics as the second order harmonic is forbidden [19]. A value of 10keV is estimated for the fluorescence X-rays. These are estimated to be present in a Gaussian beam of large width and a maximum intensity of 18% of the micro-focused beam. To calculate the probability of double counts for the 3D device the same procedure was employed but without diffusion spreading being applied. The diffusion spreading is not applied to the charge cloud in the 3D device as diffusion acts only to increase the charge cloud parallel to the pixel boundary and not across it. Therefore, the increase in charge cloud width in the 3D device does not affect the level of charge shared across pixel boundaries. The results of the simulation are compared to the experimental data in figure 13(g)–(h). The simulation reproduces the general features of the experimental data and illustrates the absence, or significant reduction, of the effect of diffusion on charge sharing in the 3D device. However, this simple simulation does not take account of capacitive coupling between pixels which may, along with uncertainty in the evaluated threshold energy applied, cause the variation between measured and simulated number of double counts.

3.6 Conclusions

A novel technique of mapping unit pixel cell responses by scanning a micro-focused X-ray beam is demonstrated. It is used to compare the response of the planar device and the 3D device to 15keV X-rays. The threshold was set to approximately half of the incoming photon energy, this

2011 JINST 6 P05002

is typical in imaging applications as it provides the best spatial resolution response of the detector along with a high detection efficiency. At lower thresholds charge shared into neighbouring pixels decreases the spatial resolution by also producing counts in pixels adjacent to the incident pixel. At higher thresholds photons incident on the pixel borders may not be counted which has the effect of shrinking the effective pixel area and decreasing the detection efficiency. The efficiency is normalised by assuming an area of full efficiency in the region far from the electrodes (shown to have an efficiency of 99.7% with pions). An effective insensitive column size of 6μm is measured in the 3D sensor which is compatible with the expectation. An efficiency of 51$\pm$ 5% is found in the region of the central electrode. An efficiency of 35$\pm$ 9% for the 3D device is measured at the pixel corners. The same efficiency, within experimental error, at the corners is measured for the planar device. Thus the loss of efficiency from the presence of the electrode column in the 3D sensor is approximately compensated by the efficiency gain from the sensor having less charge sharing than the planar device. A simple simulation to predict the amount of double counting at low thresholds is presented and the results reproduce the general features of the experimental data for both the planar and 3D devices. The model supports the hypothesis that the reduction in charge sharing in the 3D design is a result of limited lateral charge diffusion.

4 Discussion

The pixel response of novel 3D double-sided sensors has been investigated by two separate methods. A custom built telescope was used to map the pixel response to high energy pions and a micro-focussed X-ray beam mapped the response to 15keV photons. Results are compared with a standard planar device.

The high energy beam telescope provides the position of incidence of the pions on the device under test. The results from the entire detector matrix are mapped to a single pixel cell, and absolute efficiencies can be extracted. In comparison the micro-focused X-ray beam probes the response to X-rays in a selected scanned area, providing detailed information from a single pixel. The flux of photons on the detector is unknown and hence only relative efficiencies can be extracted. Currently the telescope resolution of 2.3μm gives a more exact position of the particle's point of incidence than the 4.5μm FWHM of the micro-focused beam achieved in the first study here. Since completion of this experiment it has been demonstrated that the beam size can be reduced to a FWHM of 2.2μm and the background present greatly reduced by detuning the monochromator in order to suppress higher harmonics present in the beam [20].

The X-ray testbeam at the Diamond Light Source synchrotron was conducted by a small group of the authors in four days, and the analysis completed relatively quickly. The pion testbeam required the construction of a telescope, data taking by a large number of authors, and significant software development and analysis which is reported on in the comprehensive companion paper [6]. Overall more information, and of higher accuracy, on the detector is extracted from the pion testbeam, and this method is recommended for detailed studies. However, this additional information comes at significantly greater expense than required for the Diamond Light Source tests, and their micro-focus X-ray beam facility is recommended as an effective tool for prototype detector investigations.

2011 JINST 6 P05002

A detection efficiency of 93.0 $\pm$ 0.5% across the pixel surface was measured at 20V bias at normal incidence in the pion testbeam with a threshold of approximately 1600 electrons. The regions of low efficiency have been shown in both the pion and X-ray testbeams to be restricted to the region around the electrode columns. With this low threshold set in the pion testbeam, the double-sided 3D detector, unlike in a single sided 3D detector, still shows a high efficiency (86.7$\pm$0.5%) in a region of 5μm around the pixel centre, due to charge collected in the Si above the central electrodes. The peak value of the Landau distributions obtained from the region around the central electrode is compatible with the particle having deposited charge in the 35μm silicon above the central electrode.

A measure of the inactive region around the electrodes is obtained from two methods: the first uses the efficiency measured in a region fully enclosing the loss from the electrode; the second a plot of the efficiency as a function of distance from the pixel centre. The first method was applied in both the pion and X-ray testbeams, the second in the pion testbeam only. All three values are compatible and the best estimate of the effective inactive column radius is 7.6$\pm$0.6μm. This value is compatible with that expected from the electrode column size (5μm radius) and distance of the dopant diffusion into the substrate (3μm).

In X-ray imaging applications the minimum spatial resolution, according to Nyquist sampling, is two pixels or greater. Hence sub-pixel regions of inefficiency only act to lower the overall pixel efficiency but not to degrade the resolution. However, in high energy experiments where individual particles are tracked through the detector areas of reduced efficiency are more problematic. Through rotation of the device with respect to the incident beam the effect of the columns can be removed and a detection efficiency of 99.8$\pm$0.5% is measured across the full area at 10^o with a 1600 electron threshold.

A significant reduction in the amount of charge sharing in the double-sided 3D detector is evident using both techniques. 59% of pions incident on the planar pixel detector at normal incidence leave multi-hit clusters while only 14% multi-hit clusters occur in the 3D device. A 60% drop in the amount of double counting photons at low threshold levels is also measured in the X-ray measurements. Simulation of the X-ray charge deposition suggests that the observed 3D detector results are compatible with only limited charge diffusion occurring between pixels in the 3D device.

Acknowledgments

The authors wish to thank the B16 beamline support team at the Diamond Light Source for their effort in producing a first micro-focus beam for these studies and their assistance during the data taking, and the CERN SPS and testbeam groups for their support. We would like to thank the Medipix collaboration for their help with the front-end chips and with the testbeam telescope. The authors acknowledge the useful discussions on 3D sensors with colleagues in the CERN RD50 collaboration. The double-sided 3D detector development work at the University of Glasgow was supported by grants from EPSRC and STFC, and the work at CNM has been partially supported by the Spanish Ministry of Education and Science through the GICSERV program "Access to ICTS integrated nano- and microelectronics cleanroom". The authors would also like to acknowledge the contribution made by Prof. Val O'Shea through the STFC ST/G004471/1 and EPSRC EP/G005141/1 grants.

2011 JINST 6 P05002

References

[1] S.I. Parker et al., *3D — A proposed new architecture for solid-state radiation detectors*, Nucl. Instrum. Meth. **A 395** (1997) 328.

[2] R. Bates et al., *Charge collection studies and electrical measurements of heavily irradiated 3D Double-Sided sensors and comparison to planar strip detectors*, submitted to *IEEE Trans. Nucl. Sci.* (2010).

[3] J.C. Kenney et al., *Results from 3D silicon sensors with wall electrodes: near-cell-edge sensitivity measurements as a preview of active-edge sensors*, IEEE Trans. Nuc. Sci. **48** (2010) 2405

[4] D. Pennicard, *Simulation results from double-sided 3D detectors*, IEEE Trans. Nuc. Sci. **54** (2007) 1435.

[5] M. Mathes et al., *Test beam characterization of 3D silicon pixel detectors*, IEEE Trans. Nuc. Sci. **55** (2008) 3731.

[6] A. Kazuyoshi et al., *Charged particle tracking with the timepix ASIC*, submitted to *Nucl. Instrum. Meth.* (2010) [arXiv:1103.2739v2].

[7] G. Pellegrini et al., *First double-sided 3D detectors fabricated at CNM-IMB*, Nucl. Instrum. Meth. **A 592** (2008) 38.

[8] D. Pennicard et al., *Design, simulation, production and initial characterisation of 3D silicon detectors*, Nucl. Instrum. Meth. **A 598** (2009) 67.

[9] X. Llopart et al., *Medipix2: a 64-k pixel readout chip with 55μm square elements working in single photon counting mode*, IEEE Trans. Nuc. Sci. **49** (2002) 2279..

[10] X. Llopart et al., *Timepix, a 65k programmable pixel readout chip for arrival time, energy and/or photon counting measurements*, Nucl. Instrum. Meth. **A 581** (2007) 485.

[11] Z. Vykydal et al., *USB interface for Medipix2 pixel device enabling energy and position-sensitive detection of heavy charged particles*, Nucl. Instrum. Meth. **A 563** (2006) 112.

[12] T. Holy et al., *Data acquisition and processing software package for Medipix2*, Nucl. Instrum. Meth. **A 563** (2006) 254.

[13] L. Tlustos et al., *Imaging properties of the Medipix2 system exploiting single and dual energy thresholds*, IEEE Trans. Nuc. Sci. **53** (2006) 367 [arXiv:0018.9499].

[14] J. Jakubek et al., *Pixel detectors for imaging with heavy charged particles*, Nucl. Instrum. Meth. **A 591** (2008) 155.

[15] D. Pennicard et al., *Charge sharing in double-sided 3D Medipix2 detectors*, Nucl. Instrum. Meth. **A 604** (2009) 412.

[16] B. Norlin et al., *Characterisation of the charge sharing in pixellated Si detectors with single-photon processing readout*, Nucl. Instrum. Meth. **A 563** (2006) 133.

[17] F.J. Briesmeister, *MCNP-A general Monte Carlo n-particle transport code*, LA-13709-M (2000).

[18] K. Iniewski et al., *Modeling charge-sharing effects in pixellated CZT detectors*, IEEE Nucl. Sci. Symp. Conf. Rec. **1-11** (2007) 4608.

[19] R. Caciuffo et al., *Monochromators for x-ray synchrotron radiation*, Phys. Rept. **152** (1987) 1.

[20] E.N. Gimenez et al., *Study of charge-sharing in MEDIPIX3 using a micro-focused synchrotron beam*, 2011 *JINST* **6** C01031.

2011 JINST 6 P05002